

UNIwersytet Jagielloński
Wydział Fizyki, Astronomii i Informatyki Stosowanej

Adam Strach
Nr albumu: 1163079

Inclusive η reconstruction in $\pi^+\pi^-\pi^0$ decay
channel using kinematical fitting in HADES
experiment

Praca magisterska

na kierunku Fizyka

Praca wykonana pod kierunkiem
Prof. Dr hab. Piotr Salabura

Kraków 2024

Abstract

A kinematic fit procedure was utilized to improve the resolution of measured particle track parameters in the η and ω mesons reconstruction to finally determine the inclusive production cross sections. Data have been collected in proton-proton collisions at 4.5 GeV using the HADES detector at GSI/FAIR facility in Germany in February 2022. The η and ω mesons have been reconstructed using their decays into three pions: $\eta \rightarrow \pi^+\pi^-\pi^0(\rightarrow \gamma\gamma)$, $\omega \rightarrow \pi^+\pi^-\pi^0(\rightarrow \gamma\gamma)$. The charged pions have been detected in the HADES Spectrometer, while the neutral pion with the Electromagnetic Calorimeter (ECAL) via the decay into two photons. Experimentally obtained energy resolution of ECAL has been used as a basis in the kinematic fit procedure, with a constrain to reconstruct the π^0 mass from the two decay photons. Then the results have been compared to the resolutions obtained based on dedicated Monte Carlo simulations. Finally, the procedure has been implemented for the experimental data allowing for very clean and efficient η and ω reconstruction.

I would like to express my sincere gratitude to Dr. hab. Izabela Ciepał for her invaluable help and advices, without which this thesis would not have been possible to accomplish.

I am also deeply grateful to Prof. Dr. hab. Piotr Salabura for his insightful review and valuable comments during the proofreading of this work.

A special thanks to my fiancée Martyna, whose unwavering support, understanding, and motivation gave me strength every day.

Spis treści

1	Introduction	5
1.1	η meson	5
1.2	ω meson	6
1.3	Kinematic fitting	7
1.3.1	π^0 mass constraint	8
1.3.2	Pull distributions	9
1.3.3	χ^2 statistics	9
1.4	The HADES experiment	9
1.4.1	ECAL working principle	11
1.4.2	p+p experiment	12
2	Simulations	13
2.1	π^+ and π^- selection	14
2.2	Photons selection	14
2.3	Parametrization of the ECAL resolution	15
2.3.1	Maximal cell resolution parametrization	15
2.3.2	Geometrical parametrization	16
2.3.3	Monte Carlo parametrization	16
2.3.4	Kinematic fit performance on the simulations	21
3	Data analysis	25
3.1	η and ω reconstruction	26
4	Conclusions and outlook	29

Rozdział 1

Introduction

1.1 η meson

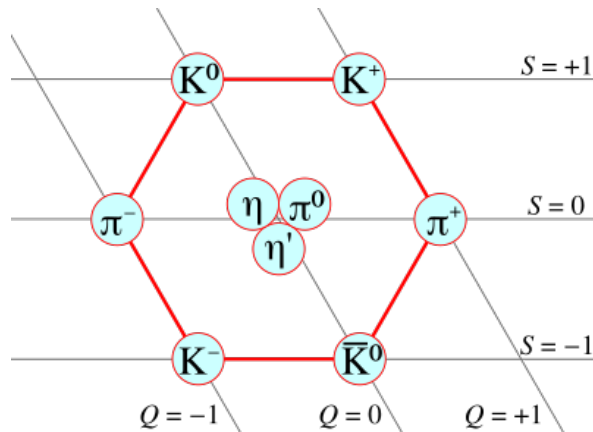
η is a neutral pseudoscalar meson. Mesons are subatomic particles that are composed of quark-antiquark pair. η is a part of nonet of spinless mesons presented in Fig. 1. It is one of the lightest mesons, with a mass of (547.862 ± 0.017) MeV [2]. The η and eta prime (η') mesons are isosinglet mesons made of a mixture of up, down and strange quarks and their antiquarks. Based on SU(3) symmetry theory, which takes into account the strong force, the quark content of η and η' mesons is as follows:

$$\begin{aligned}\eta &: \frac{1}{\sqrt{6}}(u\bar{u} + d\bar{d} - 2s\bar{s}) \\ \eta' &: \frac{1}{\sqrt{3}}(u\bar{u} + d\bar{d} + s\bar{s}).\end{aligned}\tag{1.1}$$

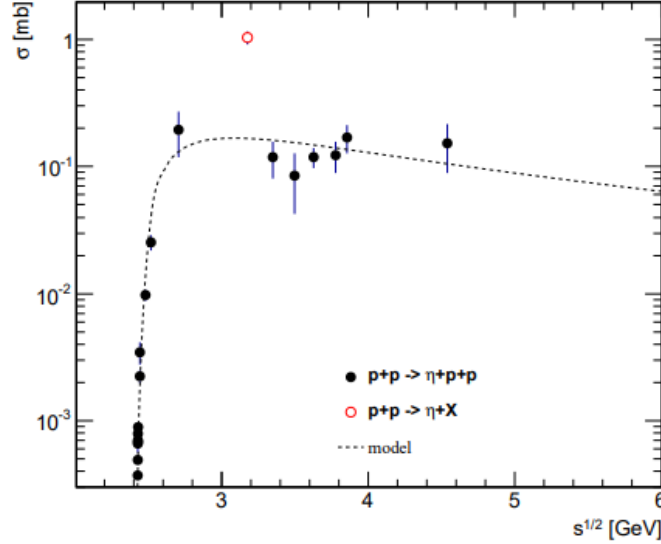
The eta meson has zero electric charge, zero isospin, zero strangeness, and its quantum numbers are $I^G(J^{PC}) = 0^+(0^{-+})$ (I, G, J, P, C denotes isospin, G-parity, total angular momentum, parity, and charge parity). Main decay channels with corresponding branching ratios[2]:

$$\begin{aligned}\eta &\rightarrow \gamma\gamma & \text{BR: } (39.41 \pm 0.20)\%, \\ \eta &\rightarrow \pi^0\pi^0\pi^0 & \text{BR: } (32.68 \pm 0.20)\%, \\ \eta &\rightarrow \pi^+\pi^-\pi^0 & \text{BR: } (22.92 \pm 0.28)\%.\end{aligned}\tag{1.2}$$

π^0 decays into $\pi^0 \rightarrow \gamma\gamma$ with branching ratio BR: $(98.823 \pm 0.034)\%$. Furthermore, many neutral and exotic mesons and some baryon resonances (N^*) decay into η , for



Rysunek 1: Nonet of spinless mesons. Figure comes from [1].



Rysunek 2: Cross sections of the η meson production in p+p collisions. The full circles illustrate the exclusive production cross sections while the red circle shows the inclusive cross section. Figure comes from [5].

example:

$$\begin{aligned}
 \eta' &\rightarrow \eta\pi^+\pi^-, \\
 a_0 &\rightarrow \eta\pi, \\
 f_1 &\rightarrow \eta\pi^+\pi^-, \\
 N^*(1520) &\rightarrow N\eta, \\
 N^*(1535) &\rightarrow N\eta.
 \end{aligned} \tag{1.3}$$

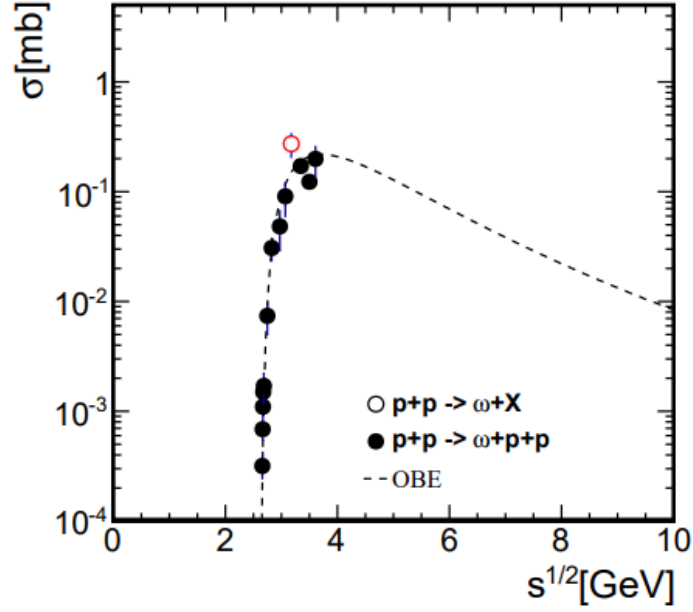
Although η meson was discovered by Pevsner et al. [3] in pion-nucleon collisions in 1961 its production mechanism is still under theoretical and experimental studies. η inclusive production cross section in proton-proton collisions at a few GeV center of mass energy (\sqrt{s}) is almost not known (there is only one data point)-see Fig.2. Knowledge of this cross section is very important for studies of di-electron (e^+e^-) invariant mass spectra in heavy-ion collisions measured with HADES. Cross sections for all sources of e^+e^- (e.g. $\pi^0 \rightarrow \gamma e^+e^-$, $\eta \rightarrow \gamma e^+e^-$) need to be fixed in order to study in-medium modification of ρ , ω vector mesons [4].

Cross section for the η production is also important parameter in the transport models to calculate p+p, p+A and A+A interactions. The world data cross sections for the η production are presented in Fig. 2. Measurement of η cross section at 4.5 GeV would improve parametrization of input parameters for such calculations.

1.2 ω meson

The ω meson is a neutral vector meson composed of a quark-antiquark pair. It has a mass of (782.65 ± 0.12) MeV [6], zero electric charge, zero isospin, zero strangeness, and its quantum numbers are 1^{--} . Main decay channel of ω is [6]:

$$\omega \rightarrow \pi^+\pi^-\pi^0, \text{ BR: } (89.2 \pm 0.7). \tag{1.4}$$



Rysunek 3: Cross sections of the ω production in p+p interactions. The full circles illustrate the measured exclusive cross sections in p+p collisions, while the red one shows the inclusive cross section. Figure comes from [5].

Similar to η , ω meson inclusive production cross sections are hardly known in this energy range. The world data for the inclusive and the exclusive production of ω are presented in Fig. 3.

The important issue of nuclear physics is to study ω interactions with nuclear matter [7],[8] and ρ - ω mixing [9]. Both aspects are connected broadly discussed subject of vector meson modification in nuclear matter [4, 10]. Furthermore, many neutral mesons and baryon resonances decay into ω :

$$\begin{aligned}\eta' &\rightarrow \omega\gamma, \\ b_1 &\rightarrow \omega\pi^+, \\ N^*(1880) &\rightarrow N\omega.\end{aligned}\tag{1.5}$$

Studies of ω and η decay parameters are also needed to develop chiral effective field theory and lattice QCD.

1.3 Kinematic fitting

Kinematic fitting for the HADES experiment has been developed by Waleed Esmail, Jenny Taylor, Malin Bohman, and Karin Schönning [11]. The algorithm uses Lagrange's multiplier method to minimize χ^2 while simultaneously satisfying one of the chosen constraints. χ^2 is calculated as:

$$\chi^2(\vec{x}) = (\vec{y} - \vec{x})^T V^{-1} (\vec{y} - \vec{x}),\tag{1.6}$$

where \vec{x} denotes the measured quantities vector, \vec{y} denotes the estimated fit quantities vector and \vec{V} is variance-covariance matrix. The constraint equation uses measured \vec{x}

and unmeasured $\vec{\xi}$ quantities vectors:

$$f(\vec{x}, \vec{\xi}) = 0. \quad (1.7)$$

Applying the Lagrange multipliers minimization method to a constraint equation 1.7, one obtains:

$$\chi^2(\vec{x}, \vec{\xi}, \vec{\lambda}) = (\vec{y} - \vec{x})^T V^{-1} (\vec{y} - \vec{x}) + 2\lambda^T f(\vec{x}, \vec{\xi}), \quad (1.8)$$

where $\vec{\lambda}$ is a vector containing Lagrange parameters. Now minimizing $\chi^2(\vec{x}, \vec{\xi}, \vec{\lambda})$ is equivalent to solving system of equation:

$$\begin{aligned} \nabla_x \chi^2 &= -2V^{-1}(\vec{y} - \vec{x}) + 2D_x^T \vec{\lambda} = 0, \\ \nabla_{\xi} \chi^2 &= 2D_{\chi}^T \vec{\lambda} = 0, \\ \nabla_{\lambda} \chi^2 &= 2\vec{f}^T = 0. \end{aligned} \quad (1.9)$$

$(D_x)_{ki} = \frac{\partial \vec{f}_k}{\partial x_i}$, $(D_{\chi})_{ki} = \frac{\partial \vec{f}_k}{\partial \xi_i}$, denotes derivative matrix of constraint equation with respect to \vec{x} and $\vec{\chi}$.

Expanding constraint function f into the Taylor series around the $(\vec{x}, \vec{\chi})$ vector while neglecting non-linear order terms we end up with an iterative procedure for solving 1.9:

$$\vec{f}_k = \vec{f}_k^v + \sum_{i=1}^N (D_x)_{ki}^v (x_i^{v+1} - x_i^v) + \sum_{j=1}^J (D_{\chi})_{kj}^v (\xi_j^{v+1} - \xi_j^v) + H.O. = 0. \quad (1.10)$$

Omitting higher order terms and rewriting sums into matrix notation:

$$\vec{f}^v + D_x^v (\vec{x}^{v+1} - \vec{x}^v) + D_{\xi}^v (\vec{\xi}^{v+1} - \vec{\xi}^v) = 0, \quad (1.11)$$

some algebraic operations lead to final formulas for updating variables:

$$\begin{aligned} r &:= \vec{f}^v + D_x^v (\vec{y} - \vec{x}^v), \\ S &:= D_x^v V (D_x^v)^T, \\ \vec{\xi}^{v+1} &= \vec{\xi}^v - (D_{\xi}^T S^{-1} D_{\xi})^{-1} D_{\xi}^T S^{-1} r, \\ \vec{\lambda}^{v+1} &= S^{-1} (r + D_{\xi} (\vec{\xi}^{v+1} - \vec{\xi}^v)), \\ \vec{x}^{v+1} &= \vec{y} - V D_x^T \vec{\lambda}^{v+1}. \end{aligned} \quad (1.12)$$

1.3.1 π^0 mass constraint

The constraint equation 1.7 can be chosen based on almost any physical or geometrical law. In the channels of interest with the π^0 decay into two photons, this condition is the mass of the reconstructed π^0 , which must be equal to the nominal π^0 mass (134.9770 ± 0.0005) $\frac{\text{MeV}}{c^2}$ (PDG). If $\vec{\gamma}_0, \vec{\gamma}_1$ are 4-vectors of the measured photons then the constraint equation is of the form:

$$g(\vec{x}, \vec{\xi}) := |\vec{\gamma}_0 + \vec{\gamma}_1| - 134.977 \frac{\text{MeV}}{c^2} = 0. \quad (1.13)$$

1.3.2 Pull distributions

If measured variable ρ change after performing the kinematic fit to y then one defines *Pull* variable as:

$$Pull := \frac{y - \rho}{\sqrt{\sigma^2(y) - \sigma^2(\rho)}}, \quad (1.14)$$

$\sigma^2(y)$, $\sigma^2(\rho)$ are variances corresponding to y and ρ . In most cases variance of a fit $\sigma^2(\rho)$ is negligible compared to $\sigma^2(y)$. If distributions of errors of variables can be assumed to be Gaussian and variances are perfectly known then the obtained *Pull* distribution would be normal. If the assumed variable variance is underestimated, then obtained *Pull* distribution would be Gaussian with standard deviation $\sigma > 1.0$ (decreased denominator of 1.14), similarly if the variance is overestimated, then pull distributions would be narrower $\sigma < 1.0$. If the fitting procedure is biased then the *Pull* distribution would also be biased (mean of distribution $\mu \neq 0$).

1.3.3 χ^2 statistics

For independent Gaussian variables X_1, X_2, \dots, X_n with corresponding means $\mu_1, \mu_2, \dots, \mu_n$ and standard deviations $\sigma_1, \sigma_2, \dots, \sigma_n$, the transformation

$$\chi^2 := \sum_{i=1}^n \frac{(X_i - \mu_i)^2}{\sigma_i^2}, \quad (1.15)$$

follows χ^2 distribution with n degrees of freedom.

In the refit procedure, χ^2 is calculated according to equation 1.6. If errors are assumed to follow uncorrelated Gaussian distribution centered at zero, n variables are fitted with k independent constraint equation, then calculated χ^2 should follow χ^2 distribution with $n - k$ degrees of freedom.

In practice more often used distribution is a χ^2 distribution transformed by applying the cumulative distribution function. The obtained distribution is often called "probability distribution". Such distribution should be uniform on $[0, 1]$. A basic rule of thumb is that it is allowed for the distribution to not be flat for low probabilities (in real data populated with background events) but should be flattening fast.

It should be noted that the probability is directly related to the χ^2 value. Lower χ^2 values indicate higher probability and higher χ^2 values indicate lower probability.

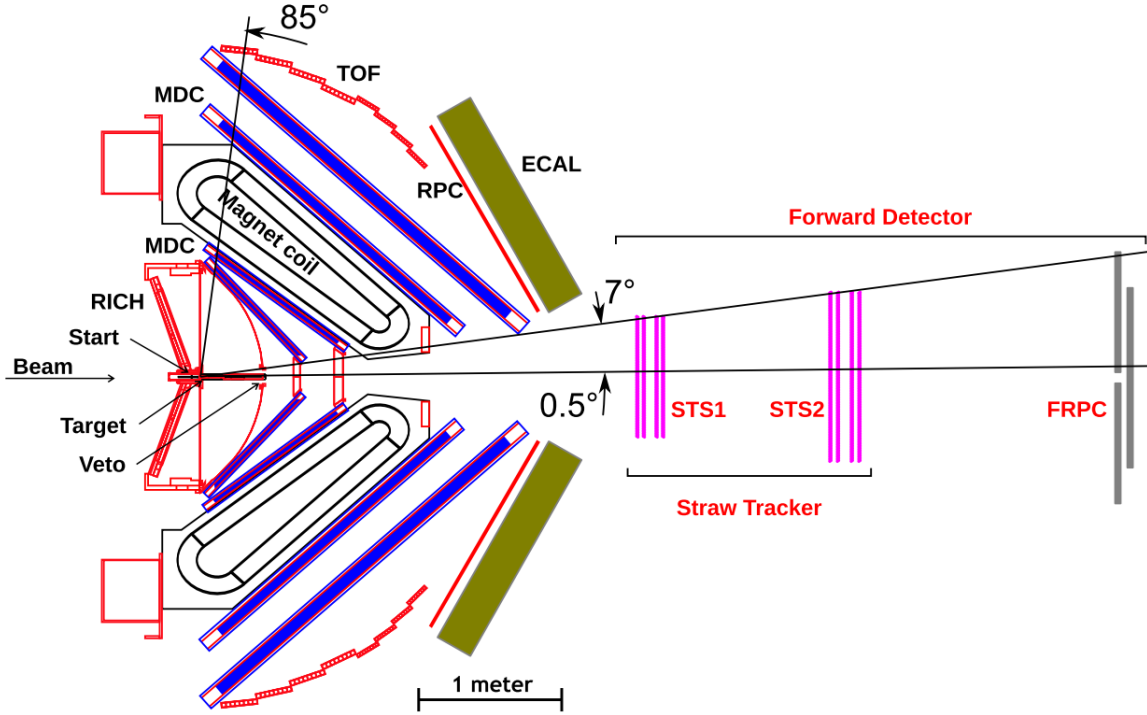
If probability distribution has a rising edge this usually means that uncertainties are over-fitted (more events with low χ^2 than expected).

If probability distribution has a falling edge this usually means that uncertainties are under-fitted (fewer events with low χ^2 than expected).

1.4 The HADES experiment

The HADES (High Acceptance DiElectron Spectrometer) is a fixed target experiment at GSI Helmholtzzentrum für Schwerionenforschung in Darmstadt. It uses high-energy beams of protons and heavy ions (*e.g.* Au+Au 1.23 AGeV collisions in 2012 run [12]) provided by SIS-18 synchrotron. For the 2022 beam time, the detection setup has been

upgraded and equipped with a new forward detector consisting of Forward Tracker and Forward Resistive Plate Chambers for TOF measurement. The HADES spectrometer has a polar angle coverage from 16° to 88° and 85% coverage of the azimuthal angle [13]. The polar angle is measured as the angle from the beam line (z-direction) and the azimuthal angle spans a plane perpendicular to the beam line (x/y plane). The Forward Tracker is capable of collecting data in the very forward polar angle range of $0.5^\circ - 7^\circ$ [14]. The whole detection setup is presented in Fig. 4.



Rysunek 4: Scheme of the HADES detector with the Forward Tracker. Graphic from [15].

The main HADES spectrometer consists of the following sub-detectors:

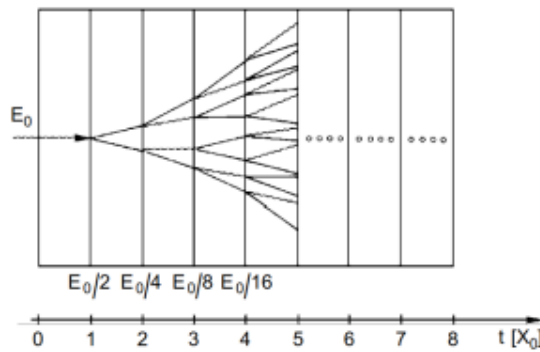
- START is a Low Gain Avalanche Diode (LGAD) based detector that allows for a precise time and position measurement [16]. It is used in heavy-ion runs, as well as in the 2022 proton-proton run, to measure the T0 reaction time [17].
- Resistive Plate Chambers (RPC) consist of 116 cells that are made of aluminum and two glass electrodes closed in SF_6 and $\text{C}_2\text{H}_2\text{F}_4$ gas mixture. The gas is ionized by charged traversing particles which creates an electron avalanche that is detected. It allows for a time of flight measurement. The RPC detector has polar angle coverage of $18^\circ < \theta < 45^\circ$.
- Time of Flight (TOF) detector contains six time-of-flight hodoscopes placed in the open sectors of the toroidal magnet. Each hodoscope consists of 22 modules which in turn consist of 8 scintillation strips closed from both sides with photomultipliers [18]. The TOF detector angular acceptance is $44^\circ < \theta < 88^\circ$.
- Ring Imaging Cherenkov (RICH) is a detector that allows for electron/positron identification using Cherenkov radiation (heavier particles are not fast enough to produce such radiation at SIS18 energies).

- Multiwire Drift Chambers (MDC) is a tracking system that allows for particle's trajectory reconstruction.
- Electromagnetic Calorimeter (ECAL) measures particle energy by detection of produced Cherenkov light that is produced by electromagnetic showers, specifically electrons and positrons, inside lead glass. It is used to detect photons. It is divided into 6 sectors each containing 163 trapezoidal modules and offers polar angle coverage of $12^\circ - 45^\circ$ [19]. For the 2022 February run, only 5 sectors of ECAL were present. More detailed principle of ECAL operation is presented in Sec. 1.4.1.
- Inner TOF (iTof) is a new detector, commissioned in 2021 which is a very important part of a new HADES trigger system. Using iTof improved the trigger selectivity and efficiency.

Technical details on the main HADES detector have been taken from [17].

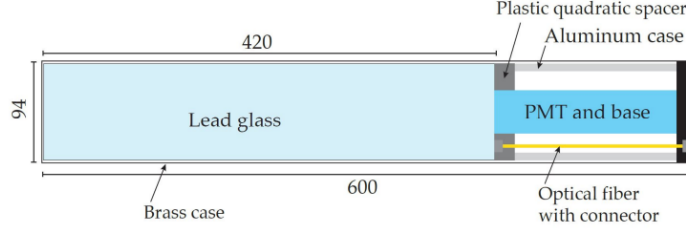
1.4.1 ECAL working principle

The electromagnetic calorimeter (ECAL) is responsible for measuring energy and position (used for trajectory reconstruction) of photons and charged particles. ECAL works on principle of electromagnetic cascades (also called showers). This cascades can be created by high energy photons or e^+ , e^- . High energy photon hits dense material of the calorimeter (in HADES it is lead glass) and creates e^+ and e^- in a pair production process. These created particles can in turn create new photons in the bremsstrahlung process. This process propagates until created photons, electrons and positrons have not sufficient energy to create further cascades. The cascade production can be monitored by observing Cherenkov light produced by high energy e^+ and e^- . This light can then be registered by Photo Multipliers Tubes (PMT). Scheme of cascade production is presented in Fig. 5. Simplified scheme of an ECAL module is presented in



Rysunek 5: Scheme depicting electromagnetic cascade production.

Fig. 6. A single module consists of two main components: lead glass and PMT, which respectively enable the creation of an electromagnetic cascade and the light detection. When high energy photon hits module near its boarder, cascade can sometimes travel to nearby module. When more than one cell recorded signal from one cascade we call this a cluster. For the light tightness each module is cased in brass. The brass coverage



Rysunek 6: Simplified scheme of the ECAL module. Figure comes from [20].

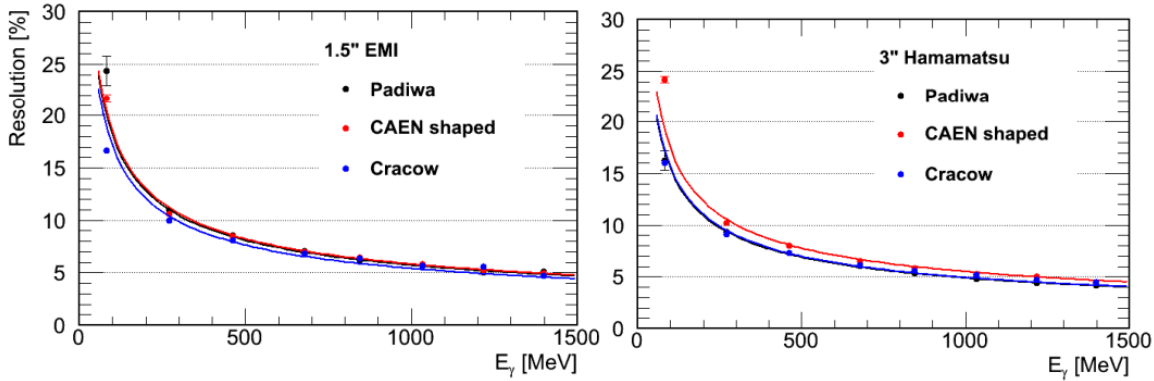
fully stops cherenkov photons from crossing cell boundaries, however some electron may still propagate cascade to nearby cells.

Following the HADES setup geometry, ECAL is divided into 6 trapezoidal sectors each in turn consisting of rows containing different amounts of modules: starting closest to the beam line 5, 5, 7, 7, 9, 9, 9, 11, 11, 13, 13, 15, 15, 17, 17.

There are two types of photomultiplier tubes (PMT) used: 3 inch Hamamatsu R6091 and 1.5 inch EMI 9903KB [21][22]. The energy resolution of used PMT depends on the energy of incoming photons:

$$\begin{aligned}\sigma_{3'} &\approx 5.5\%\sqrt{E}, \\ \sigma_{1.5'} &\approx 5.8\%\sqrt{E},\end{aligned}\tag{1.16}$$

where $\sigma_{3'}$ denotes energy resolution of Hamamatsu 3 inch PMT and $\sigma_{1.5'}$ 1.5' EMI PMT, respectively. Measured resolutions of PMTs are presented in Fig. 7.



Rysunek 7: Energy resolution of the ECAL modules. Different lines come from different electronic readouts. Plots comes from [22].

1.4.2 p+p experiment

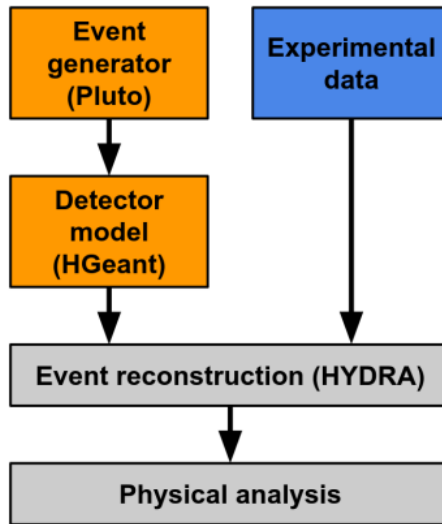
The data which are the subject of this thesis have been collected during the experimental campaign in February 2022 at the GSI/FAIR facility with the HADES spectrometer. The proton beam with a kinetic energy of 4.5 GeV was impinging on a liquid hydrogen target (cell with a length of 5 cm) containing 2×10^{23} protons. The integrated accepted luminosity of the experiment was estimated based on the elastic $p + p$ scattering and is equal to:

$$L = (6.47 \pm 0.06) \frac{1}{\text{pb}}.\tag{1.17}$$

Rozdział 2

Simulations

Monte Carlo simulations of a channel $\eta \rightarrow \pi^+\pi^-\pi^0(\rightarrow \gamma\gamma)$ has been prepared to study selection criteria and cuts optimization which subsequently will be used in the analysis of the experimental data. The simulations are also important for testing the kinematic fit performance in a controlled environment and to calculate the efficiency of the procedure. The Monte Carlo simulations have been prepared by the HADES collaboration. The general analysis framework is presented in Fig. 8. The

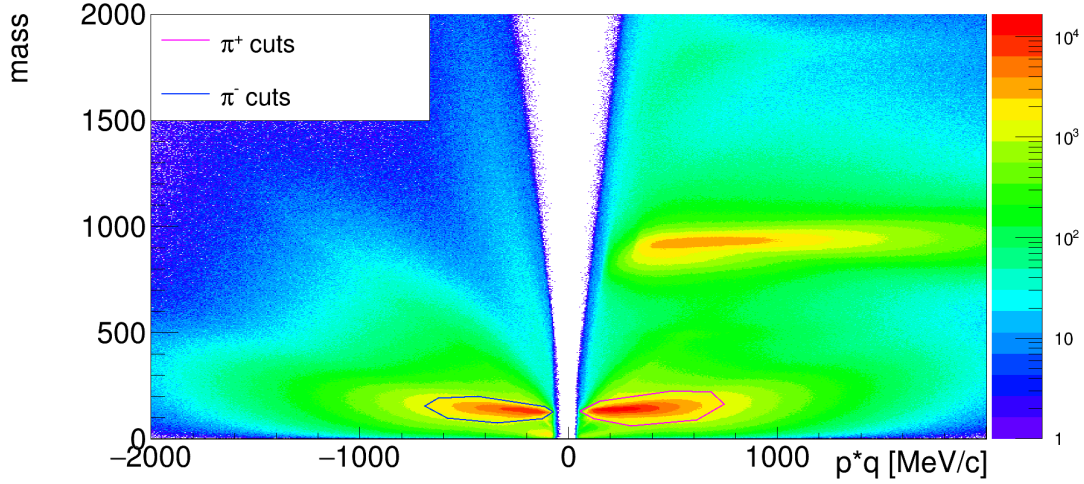


Rysunek 8: The full chain analysis of the data simulations.

η production and its decay in p+p collisions were simulated using the Pluto event generator [23]. Then particles have been processed through the virtual spectrometer (geometry implemented in the GEANT 3 environment [24]) producing the map of hits in each active detector layer. The output from GEANT is an input for the digitization and reconstruction processes handled by the HYDRA software. The data are finally stored in the *ParticleCandidates* class and contain full information from the detector e.g. tof, charge, momentum, velocity, etc.

Having reconstructed in the full simulations variables the kinematic fit procedure has been prepared and tested. A typical set of variables used in the kinematic fit implemented in the KinFit library consists of:

- $\frac{1}{p}$ - one over momentum.
- θ - polar angle.



Rysunek 9: π^+ and π^- graphical cuts presented in the *momentum – mass* spectrum. Protons contribution is also visible.

- ϕ -azimuthal angle.
- R -closest distance from track to the beamline.
- Z -the z coordinate along the beamline that is closest to the track.

Inverse momentum carries exactly the same physical information as momentum but has better convergence properties. These variables are also suitable for description of $\pi^0 \rightarrow \gamma\gamma$, however, R and Z are not used for the photons in the mass constraint.

2.1 π^+ and π^- selection

Particle identification (PID) is very important step in the data analysis. For the purpose of this study 2D graphical cuts have been implemented to select the charged pions. The purity of PID has not been studied so far.

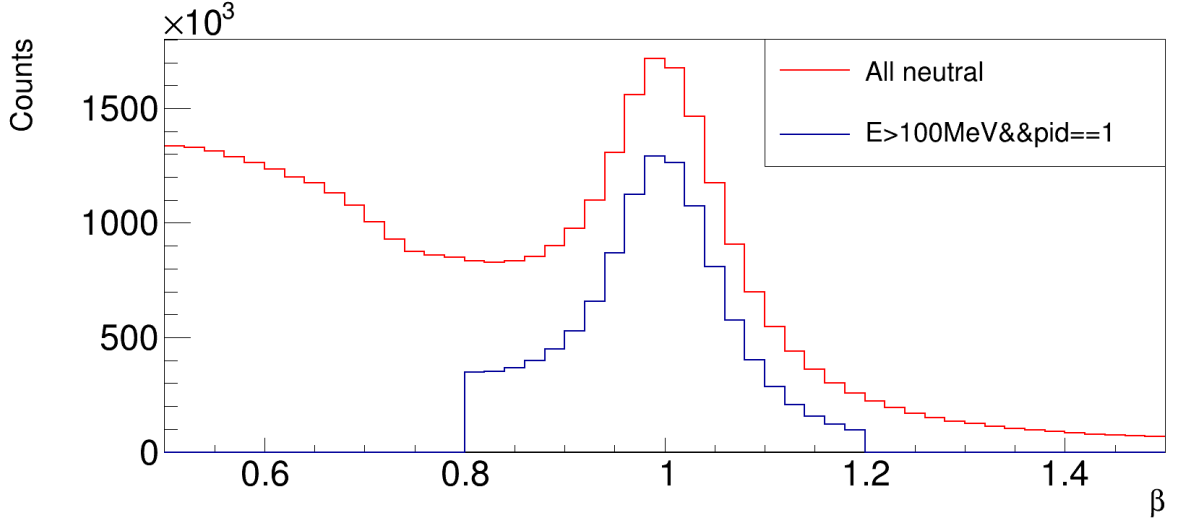
Selection of π^+ and π^- can be done based on graphical cuts on a 2D distribution of β – *momentum* or equivalently on a *momentum – mass* spectrum. β – *momentum* is transformed into *momentum – mass* by:

$$m = |p| \sqrt{\frac{1}{p^2} - 1}. \quad (2.1)$$

Spectra and cuts have been evaluated based on the Monte Carlo simulations of the $p + p \rightarrow p + p + \eta [\rightarrow \pi^+ \pi^- \pi^0]$ reaction. The obtained graphical cuts are presented in Fig. 9.

2.2 Photons selection

Besides the charged pions also photons need to be identify. The photon selection has been optimized based on the same simulation sample as mentioned in the previous Section. Photon candidates are stored in the *EmcNeutralCand* class in the HYDRA



Rysunek 10: Selection of photons with ECAL based on the velocity cut $0.8 < \beta < 1.2$.

software. Based on the reconstructed energy and velocity β , selection windows have been defined as follows: only the candidates with energy higher than 100 MeV and β in the range of 0.8-1.2 are accepted for the further analysis, see also Fig. 10. The cut on the energy are introduced to suppress neutrons in the experimental data.

The cuts are quite wide and the contributing background will be further removed by the kinematic fit constraints (probability cut).

2.3 Parametrization of the ECAL resolution

A well-established parametrization of covariance matrix V is required for the kinematic fit (see Chapter 1.3).

Three approaches for the σ_θ and σ_ϕ resolution parametrization have been considered in the analysis:

1. Maximal cell resolution parametrization,
2. Aproximated geometrical resolution parametrization,
3. Monte Carlo cell-wise parametrization.

2.3.1 Maximal cell resolution parametrization

Maximal cell resolution parametrization gives a sharp estimate on maximum of the variance. In maximal parametrization the ϕ and θ resolution is calculated assuming that distribution of θ and ϕ for photons inside a cell is uniform, then the ϕ resolution is given as:

$$\sigma_\phi = \frac{60^\circ}{N_{mod}^{row} \cdot \sqrt{12}}, \quad (2.2)$$

where N_{mod}^{row} is the number of modules in a given row. σ_ϕ ranges from 3.5° to 1° . For the θ resolution:

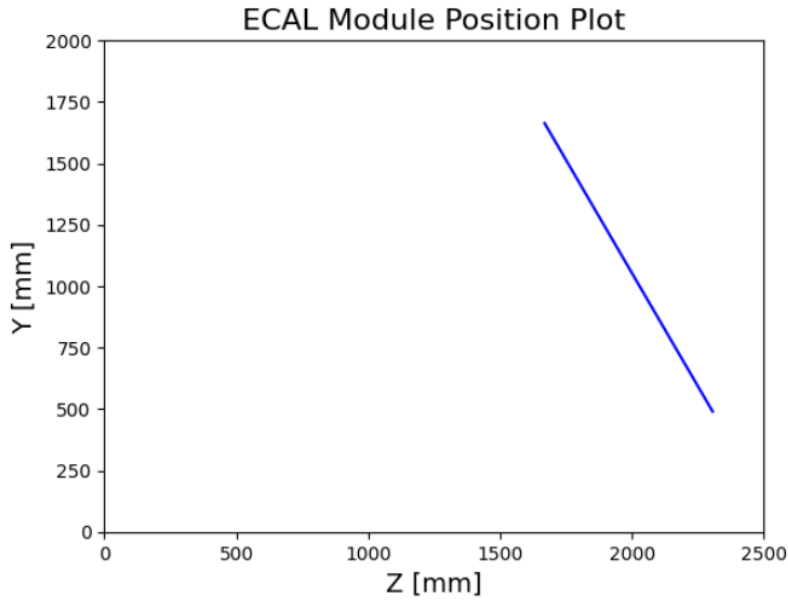
$$\sigma_\theta = \frac{27^\circ}{N_{rows} \cdot \sqrt{12}}, \quad (2.3)$$

where N_{rows} is the number of rows and 27° is in the ECAL total acceptance in the polar angle. In both cases, division by $\sqrt{12}$ comes from the standard deviation of a uniformly distributed random variable. σ_θ is approximately equal to 0.55° . In both cases, division by $\sqrt{12}$ comes from the standard deviation of a uniformly distributed random variable.

2.3.2 Geometrical parametrization

Geometrical parametrization has been prepared based on numerical calculations using Python programming language.

Errors are parametrized in a function of the θ polar angle. Firstly, one ECAL segment is parameterized in a Z-Y plane (Z is parallel to the beam direction and point (0.0) is center of the target). Such parametrization is presented in Fig. 11.



Rysunek 11: Geometrical parametrization of one ECAL segment presented for a Y direction.

Simulated photons coming from the target (0.0) at different angles θ_r hits an ECAL module. Distance calculated between the interaction point and the detection point is denoted as r . Resolution in θ for a photon incoming at a polar angle θ_r is calculated as:

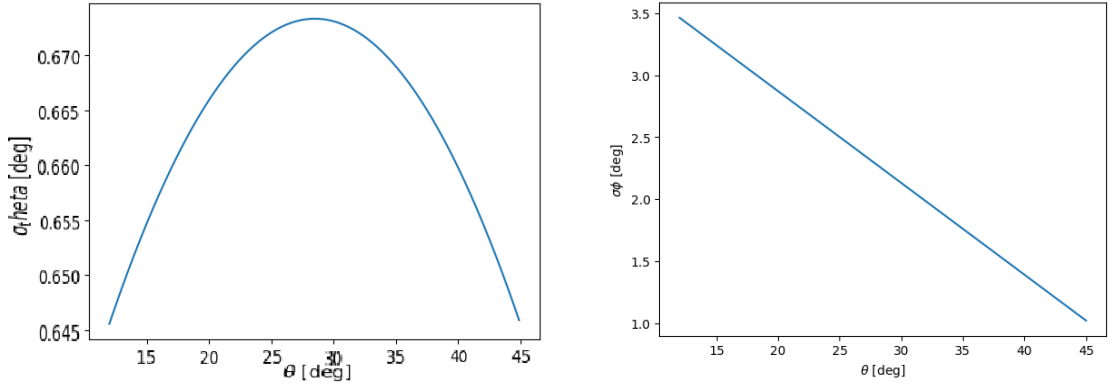
$$\sigma_\theta^{\theta_r} = \frac{a}{\sqrt{12} \cdot r_\theta} \quad (2.4)$$

$a = 92$ mm is width of a scintillation crystal in a single ECAL module.

Resolution in ϕ for particle incoming at θ_r polar angle $\sigma_\phi^{\theta_r}$ is obtained as a simple linear interpolation between lowest resolution and highest resolution (calculated as in maximal cell error). Obtained dependencies of σ_θ and σ_ϕ on θ are presented in Figs. 12.

2.3.3 Monte Carlo parametrization

Analysis of the Monte Carlo simulations allows for an independent check of the methodology and for more detailed studies of the ECAL resolution and performance.

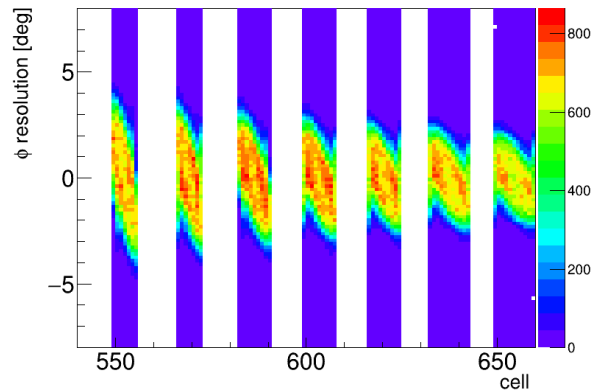


Rysunek 12: Geometrical parametrization of the resolution in θ (left plot) and ϕ (right plot) in a function of θ .

Instead of the parametrization of σ_θ and σ_ϕ in a function of θ , as it was done with the maximal error and geometrical parametrizations, it is possible and more accurate to do cell-by-cell analysis. In this approach various detector effects can be studied and taken into account like the influence of the edge cells or the dependence of the cluster size (one or more cells response to the same electromagnetic cascade, see also Sec. 1.4.1).

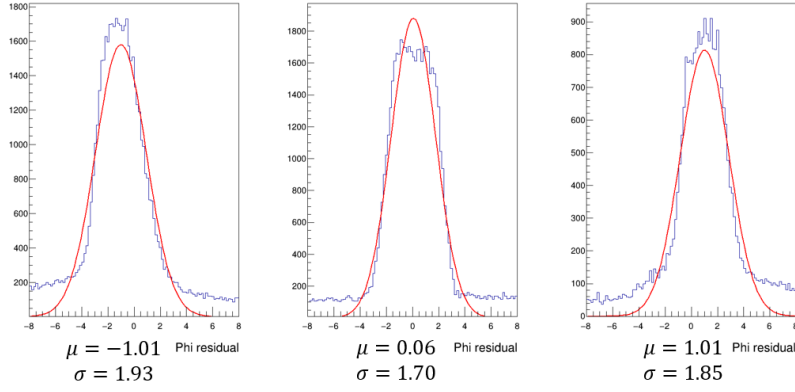
To obtain the Monte Carlo resolution parametrization the same photon selection procedure as described in Sec. 2.2 was used. Further, only the primary photons from the π^0 decay are selected. Distributions of differences of the reconstructed and true (simulated) values of θ , ϕ have been prepared for each cell individually. Energy differences has been studied in energy bins of 10 MeV. Such distributions are called residuals, or residuals distributions. Gaussian function has been fitted to each of the distribution. During this procedure, it has been observed that residuals of ϕ are systematically shifted. The larger the distance from the center of the row the shift is larger. This phenomenon is presented in a two-dimensional plot of residual vs cell number in Fig. 13. Examples of residual distributions from edge and middle cells in the same row are presented in Fig. 14.

A possible reason for this shift is an electromagnetic cascade spreading to neighboring cells, thus affecting reconstruction of incoming particles. If particle is coming with a large angle with respect to the detector plane then the electromagnetic cascade would



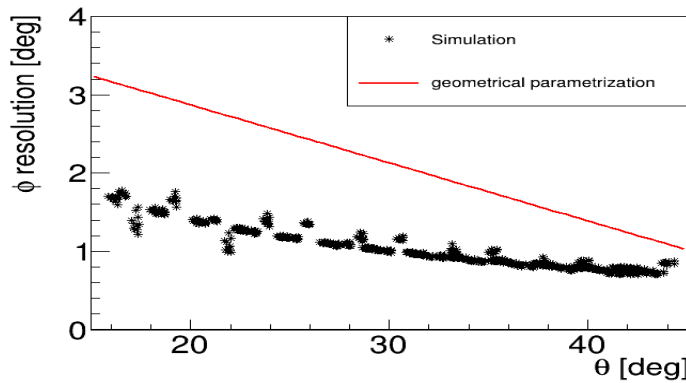
Rysunek 13: ϕ residuals versus cell number. Visible systematical shift.

also be shifted in that direction.

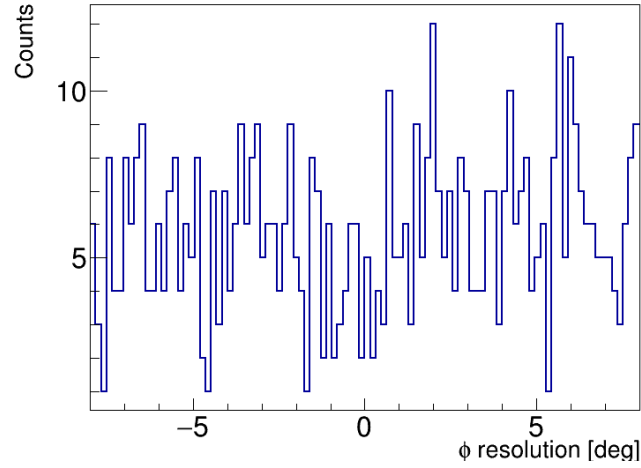


Rysunek 14: Residuals of ϕ for three different cells in the same row of ECAL. The Two distributions with means that are systematically shifted originate from edge cells (left and right plots). Correctly centered distribution (for cell placed in the center of the row) is visible in the middle plot.

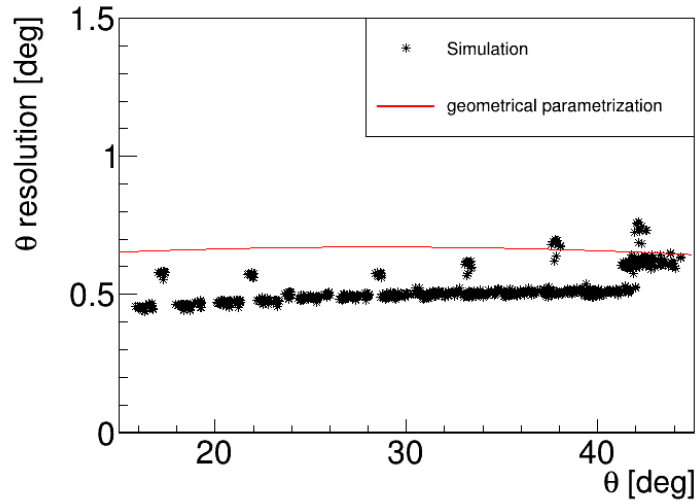
To account for such effects, a lookup table of mean values of residuals (obtained from a Gaussian fit) of each cell has been prepared. The reconstructed ϕ angle would later be shifted by this value thus correcting for this systematic effect. The obtained resolution of ϕ for each cell with respect to the θ angle corresponding to the center of that cell are presented in Fig. 15. It has been observed that the cells located in the row closest to the beam line have worst resolution, however, in the studied reaction, only a negligible amount of photons are registered in that row. In the experiment, these rows are also strongly affected by secondary neutrons and will be excluded from the analysis any way. Sample of θ residual distribution for one selected cell in the lowest row is presented in Fig. 16.



Rysunek 15: The resolution in ϕ obtained in the Monte Carlo analysis in a function of θ corresponding to the center of the cell, presented in comparison to the geometrical parametrization (red line).

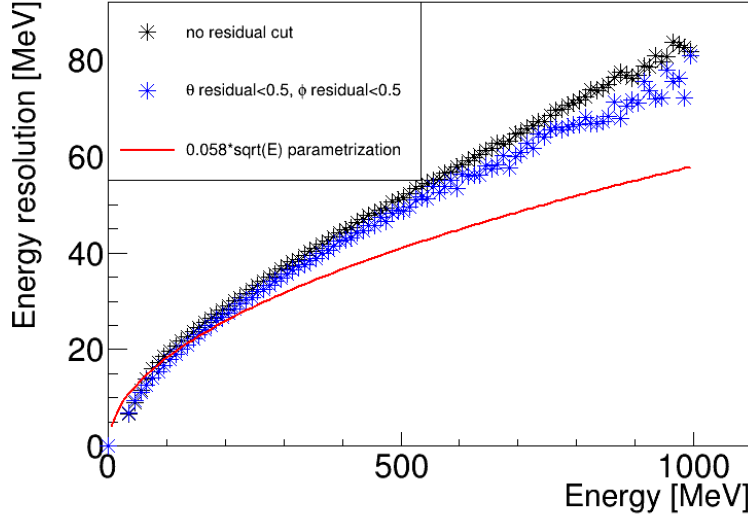


Rysunek 16: Example of residuals of θ showing poor resolution and low statistic in the lowest row of ECAL module cells.



Rysunek 17: The resolution in θ obtained in the Monte Carlo analysis in a function of θ corresponding to the center of the cell, presented in comparison to the geometrical parametrization (red line). A decrease in resolution for cells on the edges of rows is observed (so-called outlier cells).

The θ resolution does not suffer from any systematic shifts in the reconstruction. Results obtained from Gaussian fits resolutions are shown in the function of θ in Fig. 17. It has been observed that some of cells have significantly worse resolution than other ones in the same row. Upon closer examination, these outlier cells turned out to be the cells placed on the edge of a given detector sector (placed close to the supporting frames). Cells with the lower resolution in θ than obtained in the geometrical parametrization have also been excluded from the analysis.

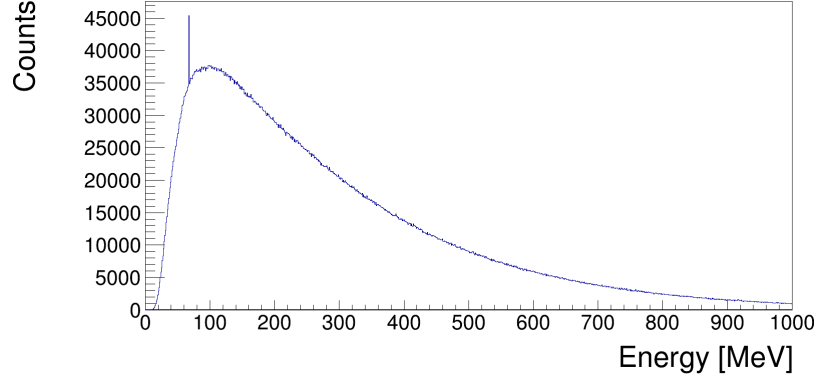


Rysunek 18: Comparison of the Monte Carlo energy resolution parametrization (black stars) to the measured one (red line) for a single ECAL module. Constraining θ and ϕ residuals (blue stars) only slightly decreases the difference between the simulated and measured resolutions.

The energy resolution in ECAL has been studied in an energy-wise (not cell-wise) way. Energy of photons have been divided into bins and for each bin a gaussian function has been fitted to the distribution of the $E_{reco} - E_{true}$ residual. The obtained energy resolution as a function of the energy is presented in Fig. 18 (black stars). This resolution has been compared to the one obtained in the measurement (red line), as it was described in Sec. 1.4.1, and presented in Fig. 7. As one can noticed with the increasing photon energy the difference between the measured and simulated resolution increase.

There can be many reasons for such discrepancy. One possible explanation is that when a photon hits the edge of the module, the resolution become worse due to the interaction with the brass casing. To test this hypothesis, the energy resolution has been calculated but on the condition that the θ and ϕ residuals must be lower than 0.5° . This requirement selects only photons that hit the center of the cell. The obtained resolution is presented in Fig. 18 as blue stars. As one can see this additional constraint does not explain the differences between measured and simulated resolutions, and brings the simulated resolution only slightly closer to the measured one. This discrepancy is still an open issue and requires further detailed investigations.

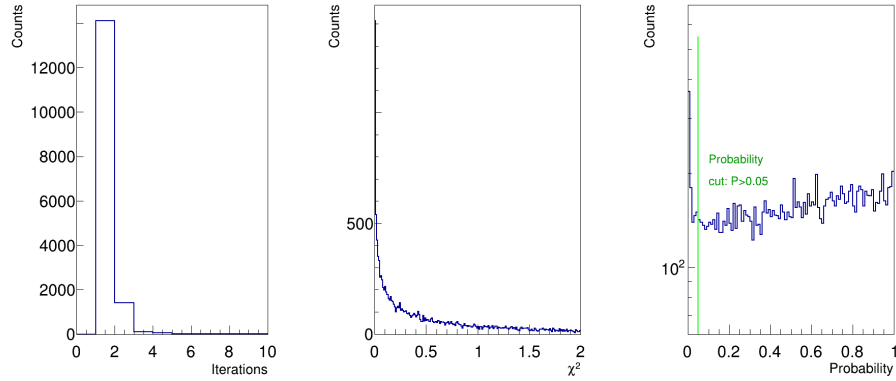
Most of the photons from the $\pi^0 \rightarrow \gamma\gamma$ reaction have quite low energy, below 400 MeV, as shown in Fig. 19, therefore this effect does not influence the final results much.



Rysunek 19: Ideal energy distribution of photons based on the simulated $\pi^0 \rightarrow \gamma\gamma$ decay. 75% of photons have energy lower than 400 MeV.

2.3.4 Kinematic fit performance on the simulations

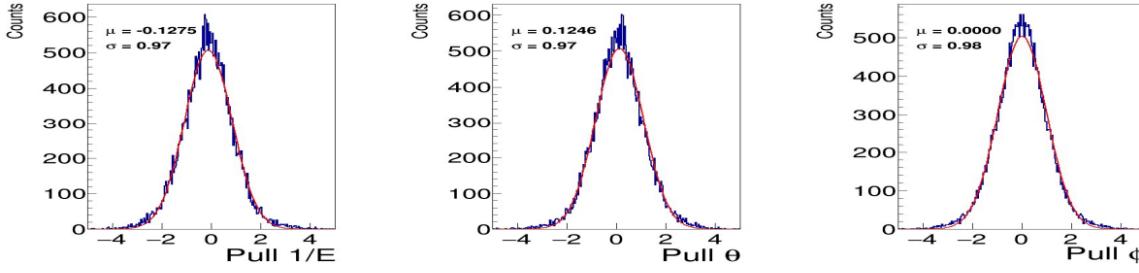
Kinematic fit performance has been tested with the simulations of $pp \rightarrow pp\eta(\rightarrow \pi^+\pi^-\pi^0)$. The event hypothesis was to search for at least 2 γ 's, at least 1 π^+ and at least 1 π^- candidates. For each photon pair characterized with the set of kinematic variables, as describe in Sec. 2, the kinematic fit procedure has been applied together with the obtained Monte Carlo resolutions (see previous Section) and the π^0 mass distribution has been reconstructed. To check the fit performance a set of



Rysunek 20: Quality plots of the kinematic fit performance: number of iterations (left plot), the χ^2 distribution (middle plot) and the probability distribution (right plot).

quality plots have been prepared, like number of iterations, χ^2 and probability distributions and they are presented in Fig. 20. Most of the events converge very fast (up to 3 iterations), χ^2 distribution looks as expected. In the probability distribution a distinctive peak close to zero represents the background events, due to this fact only events with a probability larger than 0.05 will be further analyzed (background rejection cut). Disregarding the background peak, the probability distribution is almost flat, except the higher probability values. A visible rise might be due to overestimated resolutions, or it can be a result of the non-gaussian behavior of the measured quantities.

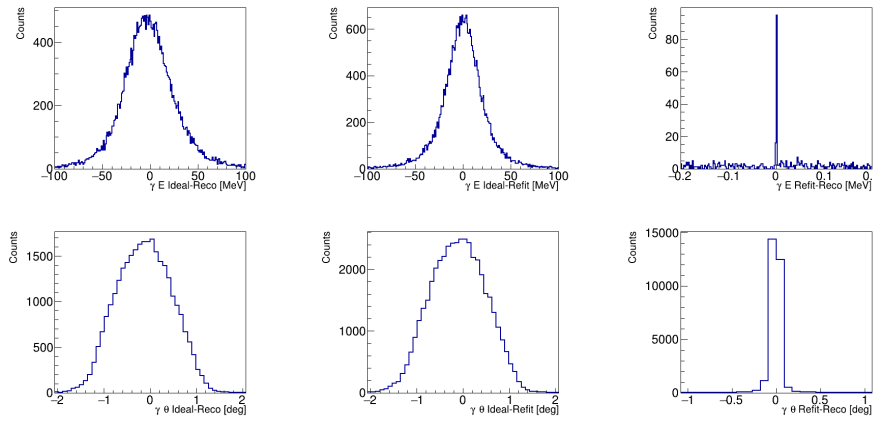
Pull distributions have been plotted according to the formula 1.14 for θ , ϕ and $1/E$, and are presented in Fig. 21. All three pull distributions are centered at zero and



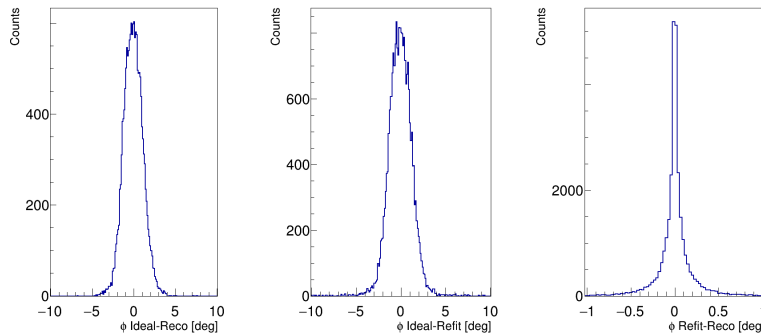
Rysunek 21: Pull distributions from simulations plotted for $1/E$ (left plot), θ (middle plot) and ϕ (right plot). All pull distributions are close to normal distributions.

have a standard deviation slightly less than one. This indicates that the resolutions are properly parametrized with a tendency to small overestimation.

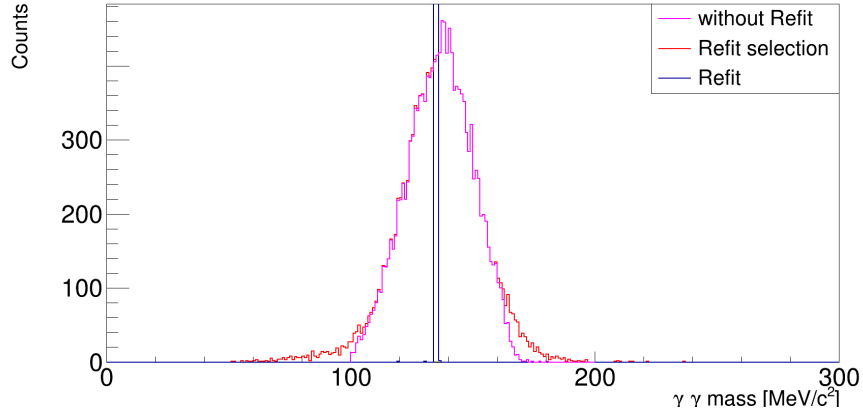
The residual distributions have also been plotted and are presented in Figs. 22 and 23. It can be seen that the residual distribution of the reconstructed and refitted quantities have non-gaussian behavior. They could be better described by a generalized Gaussian distribution, but such approach has not been, so far, implemented in the



Rysunek 22: Residual distributions for energy E and θ obtained from the Monte Carlo simulations and plotted for 3 cases: difference between ideal and reconstructed (first column), ideal and refitted (middle column) and refitted and reconstructed (right column).



Rysunek 23: Same as in Fig. 22, but for the ϕ angle.



Rysunek 24: Reconstruction of π^0 mass from the $\pi^0 \rightarrow \gamma\gamma$ decay plotted for three cases: *refit selection* (magenta) indicates reconstructed π^0 mass that fulfilled the probability cut shown in Fig. 20, *refit* (blue) shown as a reference, plotted using the refitted quantities and *without refit* (red).

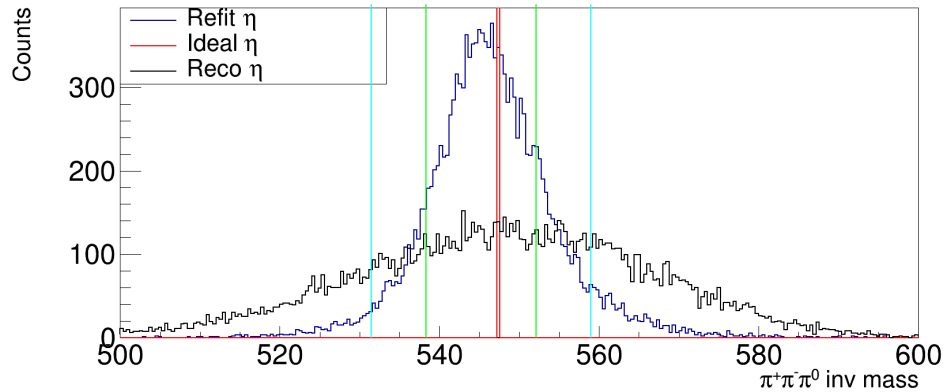
kinematic fit procedure. The non-gaussian behavior of the residuals could also explain the rise in the probability distribution shown in Fig. 20.

The reconstructed mass of π^0 is presented in Fig. 24. The refit procedure reconstructs π^0 mass at its exact value of 134.977 MeV. The refit procedure (photons from event that passed probability cut) recreates well the π^0 mass distribution, with the efficient background rejection and almost no loss in the peak region.

In the next step, the reconstructed π^0 track has been combined with π^+ and π^- tracks in order to reconstruct the η meson ($\eta \rightarrow \pi^+\pi^-\pi^0[\rightarrow \gamma\gamma]$). The reconstructed mass distribution is presented in Fig. 25. As one can notice, the refit procedure significantly improves the η mass peak resolution. The obtained η mass peak mean and the standard deviation are:

$$\mu_\eta = 544.38(45) \frac{\text{MeV}}{c^2}; \sigma_\eta = 8.82(11) \frac{\text{MeV}}{c^2}. \quad (2.5)$$

Based on the Monte Carlo simulations the reconstruction efficiency ϵ has been



Rysunek 25: Reconstructed η mass distribution. Kinematic refit significantly improves the mass resolution (compare blue and black distributions). Green and cyan lines refer to $\pm 1\sigma$ and $\pm 2\sigma$ of the corresponding Gaussian fit, respectively.

estimated, which is important parameter to calculate the inclusive production cross

sections, see Sec. 3.1. The the reconstruction efficiency has been calculated as follows:

$$\epsilon = \frac{N_{\eta}^{reco}}{N_{tot}}, \quad (2.6)$$

where N_{η}^{reco} is the final number of the reconstructed η mesons and N_{tot} is the total number of simulated $p + p \rightarrow p + p + \eta[\rightarrow \pi^+\pi^-\pi^0[\rightarrow \gamma\gamma]]$ events. The number of the reconstructed η mesons together with the calculated efficiency reconstruction are summarized in Tab. 1.

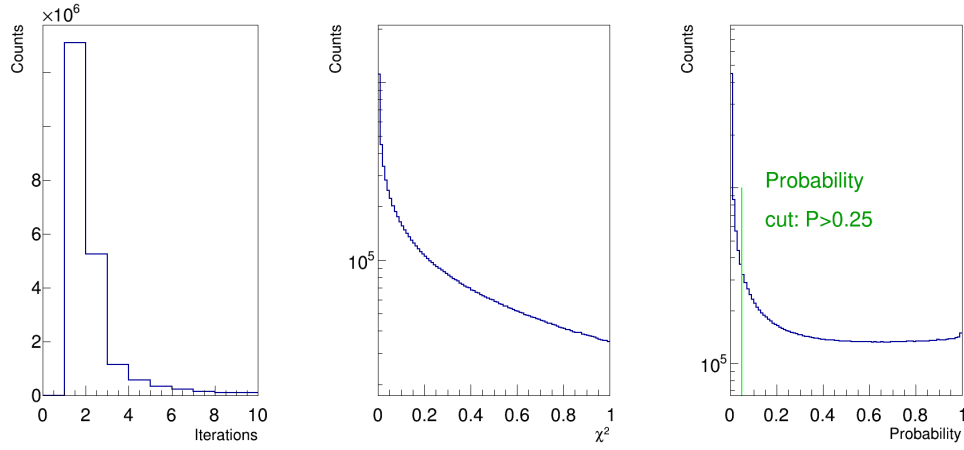
	$\pm 1\sigma$	$\pm 2\sigma$
N_{η}^{reco}	10274 ± 102	14484 ± 121
ϵ	$0.01027 \pm 0.0001 \%$	$0.01448 \pm 0.00012 \%$

Tabela 1: Number of η reconstructed in simulations in ± 1 or 2 standard deviations of the η mass peak. Total number of simulated events N_{tot} is 100 mln.

Rozdział 3

Data analysis

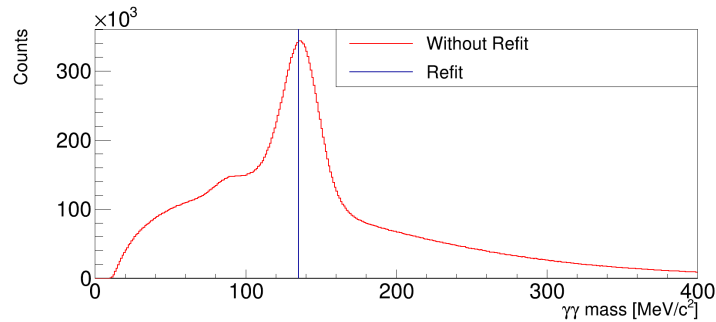
Experimental data were analyzed using the same procedure and the selection criteria as the simulations. The refit quality distributions are presented in Fig. 26. The procedure converges fast, however larger amount of events with more than 3 iterations were observed, in comparison to simulations. The probability distribution is flat, but the



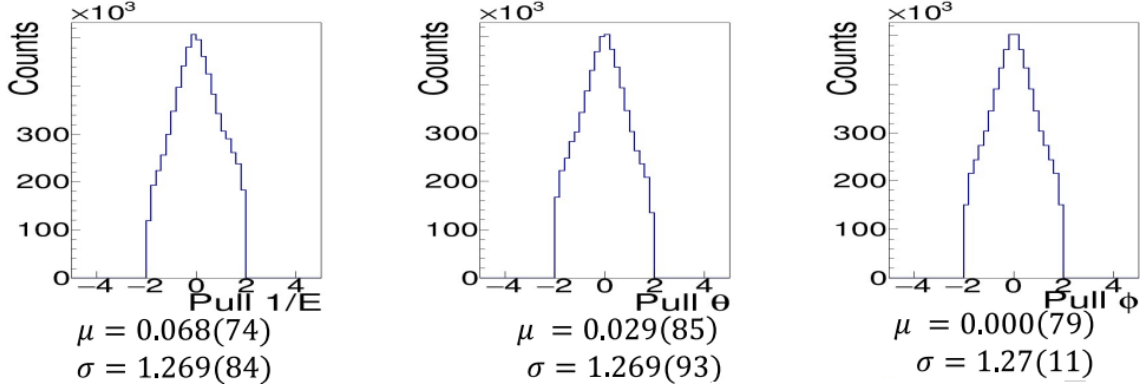
Rysunek 26: Number of iterations, χ^2 , and refit probability distribution when refit procedure was applied to experimental data.

peak at very small probability values is less pronounced compared to the simulations, making it more challenging to select an optimal probability cut condition. Consequently only events with a probability higher than 0.05 were selected for the further analysis.

Reconstructed π^0 from the selected events is presented in Fig. 27. It shows that the



Rysunek 27: π^0 mass distribution from events selected by refit procedure.



Rysunek 28: Pull distributions plotted after the probability cut for the experimental data. Standard deviation larger than 1.0 suggest an underestimation of the resolution. Sharp edges at ± 2 come from the probability cut.

π^0 mass peak without refit is reconstructed at the correct mass position.

Pull distributions are presented in Fig. 28. They are centered at zero, and have a Gaussian shape, but have a standard deviation of approx. 1.25. A sharp edges around ± 2.0 in the distributions are a result of the probability cut (low probability-large pull).

3.1 η and ω reconstruction

A mass distribution of the η and ω candidates are presented in Fig. 29. Outside of η and ω peaks region ($\pm 2\sigma$ from the peak), polynomials of the 3rd degree have been fitted to describe the background contribution. Then the background has subtracted and the Gaussian function has been fitted to the obtained signal peaks. The results are presented in Fig. 29. The obtained from the Gaussin fit η and ω peaks parameters are presented in Tab. 2. η mass peak position is reconstructed at the correct PDG value of $547.862(17) \frac{\text{MeV}}{c^2}$, but the ω mass peak is shifted from it's PDG mass $782.65(12) \frac{\text{MeV}}{c^2}$.

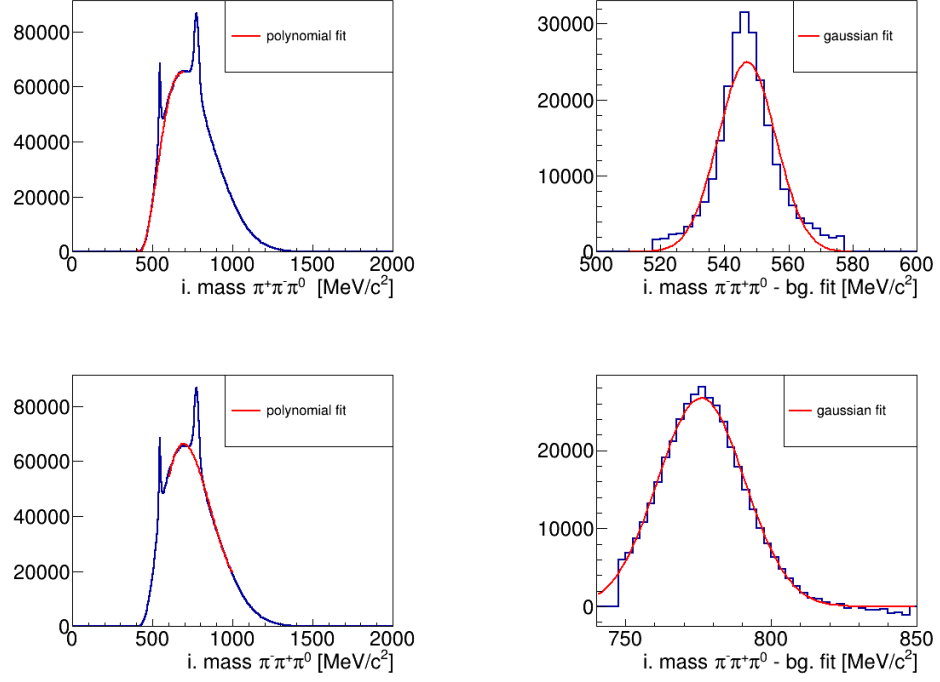
	η	ω
mean	$(547.26 \pm 0.10) \frac{\text{MeV}}{c^2}$	$(776.77 \pm 0.14) \frac{\text{MeV}}{c^2}$
standard deviation	$(9.30 \pm 0.10) \frac{\text{MeV}}{c^2}$	$(15.00 \pm 0.12) \frac{\text{MeV}}{c^2}$

Tabela 2: Obtained from fitting Gaussian function mean and standard deviation of mass peaks of η and ω . Only Gaussian fitting error is presented.

Having the signal extracted (see Fig. 29, left column), the Gaussian function has been fitted. The number of entries in $\pm 1\sigma$ or $\pm 2\sigma$ from the peak position correspond to the inclusive cross sections for the η and ω production. The cross sections have been calculated from the formula:

$$\sigma_{tot} = \frac{N}{L \cdot Br \cdot \epsilon}, \quad (3.1)$$

where N is the number of η/ω events integrated in the $\pm 1\sigma$ or $\pm 2\sigma$, $L = (6.47 \pm 0.06) \frac{1}{\text{pb}}$ is the total integrated luminosity and ϵ is the reconstruction efficiency calculated as in Eq. 2.6. Uncertainty of inclusive cross section has been calculated using mean squared error propagation formula:



Rysunek 29: Left column: η and ω mass distributions drawn together with 3rd degree polynomial functions which describe the background contributions. Right column: the signal obtained after the background subtraction.

$$\Delta(\sigma_{tot}) = \sqrt{\left(\frac{\Delta(N)}{L \cdot Br \cdot \epsilon}\right)^2 + \left(\frac{N \cdot \Delta(L)}{L^2 \cdot Br \cdot \epsilon}\right)^2 + \left(\frac{N \cdot \Delta(Br)}{L \cdot Br^2 \cdot \epsilon}\right)^2 + \left(\frac{N \cdot \Delta(\epsilon)}{L \cdot Br \cdot \epsilon^2}\right)^2}, \quad (3.2)$$

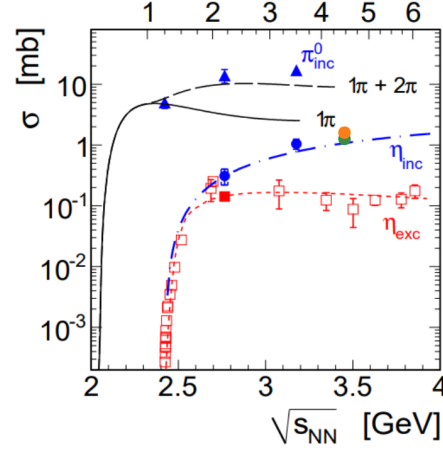
where $\Delta(N) = \sqrt{N}$ is uncertainty of the number of reconstructed η/ω particles, assuming it follows Poisson distribution. Systematic error of N has not been analyzed so far. $\Delta(L) = 0.05 \frac{1}{(\text{pb})}$ is uncertainty of the luminosity, $\Delta(Br)$ is uncertainty of η/ω branching ratio of decay into $\pi^+\pi^-\pi^0$ provided by PDG[2][6] (see 1.2 and 1.4). $\Delta(\epsilon)$ is the uncertainty of the efficiency calculated as described in Sec. 2.3.4. The numbers of the reconstructed mesons and the corresponding inclusive cross sections are summarized in Tab. 3.

	$\pm 1\sigma$	$\pm 2\sigma$
Observed number of η	176000 ± 18000	226000 ± 23000
Observed number of ω	371000 ± 38000	479000 ± 49000
σ_η	$1.15 \pm 0.12 \text{ mb}$	$1.72 \pm 0.18 \text{ mb}$
σ_ω	$0.381 \pm 0.040 \text{ mb}$	$0.573 \pm 0.060 \text{ mb}$

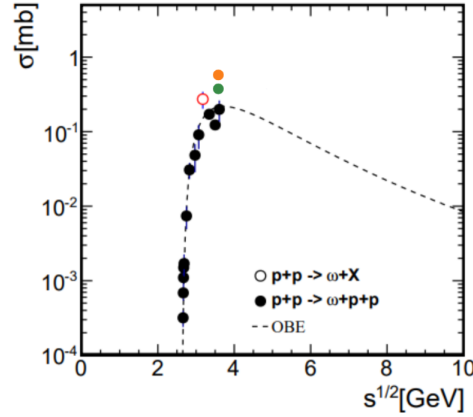
Tabela 3: Number of the reconstructed η and ω in ± 1 and 2 standard deviations from the mass peak and the corresponding cross sections. Only statistical error are given.

The obtained η/ω inclusive production cross sections are presented together with the existing world data in Fig. 30 and Fig. 31. In the case of the η cross section our results are consistent with the parametrization of inclusive η cross section proposed in [25]. The ω cross section is slightly higher than the world data (see Fig. 31), however,

these results are very preliminary and will be improved. What is more, detailed studies of systematic errors will be performed.



Rysunek 30: The cross sections for π^0 and η production in proton-proton collisions measured at various \sqrt{s} . Full green and orange circles represent the results obtained in pp@4.5 GeV with HADES for $\pm 1\sigma$ and $\pm 2\sigma$, respectively, see Tab. 3. The HADES data at energies of 1.25 [26], 2.2 [27] and 3.5 [5] GeV are presented as solid triangles and solid circles and the solid square. The dot-dashed blue curve is the parametrization of inclusive η production from [25]. Figure adopted from [27].



Rysunek 31: The cross sections for ω production in proton-proton collisions measured at various \sqrt{s} . Full green and orange circles represent the results obtained in pp@4.5 GeV with HADES for $\pm 1\sigma$ and $\pm 2\sigma$, respectively (see Tab. 3). The red empty circle is the HADES result obtained in pp@3.5 GeV. The dashed curve refers to the OBE calculations for the exclusive channels [25]. Figure adopted from [5].

Rozdział 4

Conclusions and outlook

Precise studies of the ECAL resolution have been performed cell-wise and energy-wise. This allowed one to detect systematic effects as shifts in ϕ and discrepancies between measured and observed energy resolutions. It was possible to correct for the shift in ϕ which resulted in the improvement in the kinematic fit performance. There is still unresolved problem with the discrepancy between the simulated and measured resolutions which is probably due to the cluster formation effect. As it was investigated the discrepancy become larger with the increasing photon energy. To understand this effect more detailed analysis is needed.

In the studied reactions $p+p \rightarrow p+p+\eta[\rightarrow \pi^+\pi^-\pi^0[\rightarrow \gamma\gamma]]$ and $p+p \rightarrow p+p+\omega[\rightarrow \pi^+\pi^-\pi^0[\rightarrow \gamma\gamma]]$ the implemented kinematic fit significantly improves the resolution in the η and ω mesons reconstruction and corresponding signal-to-background ratios.

The η mass peak is observed at correct PDG mass, however the ω mass peak center is almost $6 \frac{\text{MeV}}{c^2}$ off from its PDG mass. Reason for that could be due to adjusting refit procedure to the Monte Carlo simulations for the η channel, but also a fact that ω mass peak is located on top of background peak making it harder to correctly fit and subtract the background. Here, more detailed studies of the systematic effects due to the background subtraction are needed.

The obtained η and ω preliminary cross sections are in a good agreement with the former measurements and the theoretical parametrization of the inclusive production [25]. In this analysis only statistical error has been included and also extensive studies of systematical effects are needed.

These studies will be continued in the upcoming future and the most important goal is to obtain multi-differential cross sections for η and ω . In addition to that, more detailed studies of the ECAL efficiency are needed using a well-defined di-electrons sample. Correction for the acceptance need to be also evaluated in a multi-dimensional way. There are also plans to study the η' production in its decay channel $\eta\pi^+\pi^-$ with the η reconstruction using the kinematic fit procedure presented in this work and if statistics allows also its angular distribution.

The physics cases which are discussed in this thesis are a part of a large HADES experimental program focused on studies of the light neutral mesons production, decays and structure in pp @ 4.5 GeV. The main goal of the pp measurement was to study radiative and hadronic hyperon decays (Λ , Σ), production of double strangeness ($\Xi(1321)$, $\Lambda\Lambda$), hidden strangeness (φ) and inclusive di-electron production as reference for p+A and heavy-ion data.

Bibliography

- [1] Wikipedia contributors. *Meson* --- *Wikipedia, The Free Encyclopedia*. [Online; accessed 26-August-2024]. 2024. URL: <https://en.wikipedia.org/w/index.php?title=Meson&oldid=1235524526>.
- [2] M. Tanabashi and others (Particle Data Group). “Review of Particle Physics”. In: *Physical Review D* 98 (3 2018), p. 030001. DOI: 10.1103/PhysRevD.98.030001.
- [3] et al. Pevsner. “Evidence for a Three-Pion Resonance Near 550 Mev”. In: *Phys. Rev. Lett.* 7 (11 Dec. 1961), pp. 421–423. DOI: 10.1103/PhysRevLett.7.421. URL: <https://link.aps.org/doi/10.1103/PhysRevLett.7.421>.
- [4] HADES Collaboration. In: *Nat. Phys.* 15 (2019), p. 1040. DOI: <https://doi.org/10.1038/s41567-019-0583-8>.
- [5] The HADES Collaboration. “Inclusive dielectron spectra in p+p collisions at 3.5 GeV kinetic beam energy”. In: *The European Physical Journal A* 48.5 (May 2012). ISSN: 1434-601X. DOI: 10.1140/epja/i2012-12064-y. URL: <http://dx.doi.org/10.1140/epja/i2012-12064-y>.
- [6] K. Nakamura and others (Particle Data Group). “Review of Particle Physics”. In: *J. Phys. G* 37 (7A 2010), p. 075021. URL: <http://pdg.lbl.gov>.
- [7] A. Ramos et al. “The width of the ρ meson in the nuclear medium”. In: *The European Physical Journal A* 49.11 (Nov. 2013). ISSN: 1434-601X. DOI: 10.1140/epja/i2013-13148-x. URL: <http://dx.doi.org/10.1140/epja/i2013-13148-x>.
- [8] Horst Lenske. “Interactions of ω mesons in nuclear matter and with nuclei”. In: *The European Physical Journal A* 59.10 (Oct. 2023). ISSN: 1434-601X. DOI: 10.1140/epja/s10050-023-01129-x. URL: <http://dx.doi.org/10.1140/epja/s10050-023-01129-x>.
- [9] H.B. O’Connell et al. “Rho-omega mixing, vector meson dominance and the pion form-factor”. In: *Progress in Particle and Nuclear Physics* 39 (1997), pp. 201–252. ISSN: 0146-6410. DOI: [https://doi.org/10.1016/S0146-6410\(97\)00044-6](https://doi.org/10.1016/S0146-6410(97)00044-6). URL: <https://www.sciencedirect.com/science/article/pii/S0146641097000446>.
- [10] ALICE Collaboration. “Unveiling the strong interaction among hadrons at the LHC”. In: *Nature* 558 (Dec. 2020), pp. 232–238. DOI: <https://doi.org/10.1038/s41586-020-3001-6>.
- [11] Waleed Esmail et al. “KinFit: A Kinematic Fitting Package for Hadron Physics Experiments”. In: *Computing and Software for Big Science* 8.1 (Jan. 2024), p. 3. ISSN: 2510-2044. DOI: 10.1007/s41781-023-00112-x. URL: <https://doi.org/10.1007/s41781-023-00112-x>.

- [12] Behruz Kardan. “Collective flow measurements with HADES in Au+Au collisions at 1.23A GeV”. In: *Nuclear Physics A* 967 (Nov. 2017), pp. 812–815. DOI: 10.1016/j.nuclphysa.2017.05.026.
- [13] G. Agakishiev et al. “The High-Acceptance Dielectron Spectrometer HADES”. In: *Eur. Phys. J. A* 41 (2009), pp. 243–277. DOI: 10.1140/epja/i2009-10807-5. arXiv: 0902.3478 [nucl-ex].
- [14] Narendra Rathod et al. “Hyperon Studies and Development of Forward Tracker for HADES Detector”. In: *Acta Physica Polonica B* 51 (Jan. 2020), p. 239. DOI: 10.5506/APhysPolB.51.239.
- [15] HADES collaboration and PANDA@HADES collaboration. “Production and electromagnetic decay of hyperons: a feasibility study with HADES as a phase-0 experiment at FAIR”. In: *The European Physical Journal A* 57.4 (Apr. 2021), p. 138. ISSN: 1434-601X. DOI: 10.1140/epja/s10050-021-00388-w. URL: <https://doi.org/10.1140/epja/s10050-021-00388-w>.
- [16] W. Krüger et al. “LGAD technology for HADES, accelerator and medical applications”. In: *Nuclear Instruments and Methods in Physics Research Section A: Accelerators, Spectrometers, Detectors and Associated Equipment* 1039 (2022), p. 167046. ISSN: 0168-9002. DOI: <https://doi.org/10.1016/j.nima.2022.167046>. URL: <https://www.sciencedirect.com/science/article/pii/S0168900222004697>.
- [17] The HADES collaboration. “The high-acceptance dielectron spectrometer HADES”. In: *The European Physical Journal A* 41.2 (July 2009), pp. 243–277. DOI: 10.1140/epja/i2009-10807-5. URL: <https://doi.org/10.1140%2Fepja%2Fi2009-10807-5>.
- [18] N. V. Rabin, D. A. Vasil’ev, and S. V. Vladimirov et. al. “A time-of-flight measurement system for the HADES wide-aperture dielectron spectrometer”. In: *Instruments and Experimental Techniques* 43.4 (July 2000), pp. 435–452. ISSN: 1608-3180. DOI: 10.1007/BF02758944. URL: <https://doi.org/10.1007/BF02758944>.
- [19] Petr Chudoba et al. “Commissioning of the electromagnetic calorimeter ECAL of the HADES experiment”. In: Sept. 2020.
- [20] Alexandr Prozorov. “Neutral Meson Production in Ag+Ag Collisions at 1.58 A GeV with HADES Electromagnetic Calorimeter”. Doctoral Thesis. Nuclear Physics Institute CAS, 2023.
- [21] A Shabanov et al. “Calibration of the electromagnetic calorimeter ECal of the HADES experiment”. In: *Journal of Physics: Conference Series* 1667 (Oct. 2020), p. 012039. DOI: 10.1088/1742-6596/1667/1/012039.
- [22] O. Svoboda et al. “Verification of Electromagnetic Calorimeter Concept for the HADES spectrometer”. In: *J. Phys. Conf. Ser.* 599.1 (2015). Ed. by Marco Destefanis et al., p. 012026. DOI: 10.1088/1742-6596/599/1/012026.
- [23] I. Froehlich. *Pluto: A Monte Carlo Simulation Tool for Hadronic Physics*. 2007. arXiv: 0708.2382 [nucl-ex]. URL: <https://arxiv.org/abs/0708.2382>.
- [24] R Brun et al. *GEANT 3: user’s guide Geant 3.10, Geant 3.11; rev. version*. Geneva: CERN, 1987. URL: <https://cds.cern.ch/record/1119728>.

- [25] W. Cassing A. Sibirtsev and U. Mosel. In: *Z. Phys. A* 358 (1997), p. 357. DOI: <https://doi.org/10.1007/s002180050339>.
- [26] G. Agakishiev et al. In: *Phys. Lett. B* 690 (2010), p. 118.
- [27] G. Agakishiev et al. In: *Phys. Rev. C* 85 (2012), p. 054005. DOI: <https://doi.org/10.1103/PhysRevC.85.054005>.